Research Article
Vol. 43, No. 1 / January 2026 / *Journal of the Optical Society of America A* 1

Journal of the Optical Society of America A
OPTICS, IMAGE SCIENCE, AND VISION

Method of field expansions for doubly layered media with a quasiperiodic interface

David P. Nicholls

Department of Mathematics, Statistics, and Computer Science, University of Illinois at Chicago, Chicago, Illinois 60607, USA (davidn@uic.edu)

Received 14 July 2025; revised 9 November 2025; accepted 16 November 2025; posted 17 November 2025; published 3 December 2025

Periodic structures play a crucial role in applied optics; however, generalized forms of periodicity are becoming increasingly important in electromagnetics. Due not only to their importance but also to the high cost and great difficulty in producing these at the nanoscale required, numerical simulation of these devices is of extraordinary importance. In this contribution, the author derives, implements, and validates the generalization of a high-order perturbation of surface (HOPS) algorithm (the method of field expansions—FE) for the numerical simulation of layered media scattering to account for quasiperiodic interfaces. Due to their interfacial character, these HOPS approaches are substantially faster than their volumetric counterparts such as finite difference or finite element methods. Additionally, our approach can address structures that the classical FE method would find onerous (for interfaces with widely disparate periods) or impossible (for profiles of incommensurate periods) due to its enhanced capability of simulating quasiperiodic interfaces. Beyond validating the implementation, the author also investigates the (nonlinear) dispersion relation of surface plasmon resonances on a sequence of increasingly challenging vacuum–silver structures featuring a quasiperiodic interface.

https://doi.org/10.1364/JOSAA.573428

1. INTRODUCTION

The periodic patterning of structures plays a critical role in applied optics, with photonic crystals as a particularly successful example [1,2]. With these precisely structured materials, one can design band structures, specifically tailor reflectance and transmittance, and essentially manipulate the propagation of light as one wishes. Beyond this, other forms of periodicity play important roles in electromagnetics, with the surface plasmon resonances (SPRs) induced by metallic diffraction gratings [3–5] being an example of particular interest, due not only to their theoretical interest but also their practical importance, e.g., as sensors [6–12].

With the overwhelming importance of such devices, it is not surprising that the entire array of classical algorithms has been brought to bear upon the numerical simulation of these structures [13,14]. This includes the finite difference time domain (FDTD) method [15], the finite difference frequency domain (FDFD) method [16], the finite element method [17], and the discontinuous Galerkin method [18]. Other methods have been devised specifically for the governing Maxwell (Helmholtz) equations, including the planewave eigensolver [19,20], the rigorous coupled-wave analysis (RCWA) [21,22], the Fourier modal method (FMM) [23], and the discrete dipole method [24]. While each of these can be a compelling approach for quite general structures, their *volumetric* character renders them non-competitive for the SPR geometries we consider here, which feature homogeneous layers of material separated by sharp interfaces. In these cases, *surface* methods are more efficient, and primary among these are the boundary integral method [25], the boundary element method [26,27] (accelerated by the fast multipole method [28–30]), and the method of moments [31].

Of special relevance to the current research are the interfacial high-order perturbation of surface (HOPS) methods: The method of operator expansions (OEs) due to Milder [32–37], the method of field expansions (FEs) due to Bruno and Reitich [38–43], and the method of transformed field expansions (TFEs) due to the author and Reitich [44–50]. This latter method has been significantly enhanced to accommodate multiple layers and the full three-dimensional vector Maxwell equations by He, Min, Shen, and the author [51,52] and Hong and the author [53–55], and rigorously numerically analyzed in [56,57]. These approaches have been demonstrated to be rapid, robust, and reliable in their capabilities of simulating scattering returns by layered media with sharp interfaces. Due to their perturbative nature, these HOPS schemes perform best for interfaces that are small (in amplitude and/or slope) and smooth (e.g., analytic). However, they can also be applied to large and rough (e.g., Lipschitz) interfaces with numerical analytic continuation techniques (e.g., Padé summation [58]). This capability is justified by the rigorous results [46,48], which demonstrate that perturbations of *arbitrary* size can be accommodated provided that they are *real*.

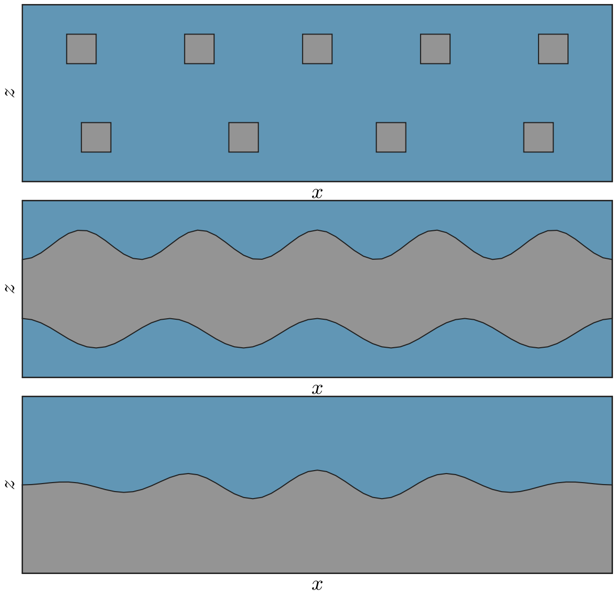

Fig. 1. (Top) Depiction of the mismatched one-dimensional subwavelength photonic crystal slabs studied in [66]. (Middle) Plot of a triply layered structure with sinusoidally corrugated layer interfaces that have mismatched periodicities. (Bottom) Plot of a doubly layered structure with a sinusoidally corrugated layer interface that is the "average" of the interfaces just above.

While the periodicity of these structures is crucial to generating the phenomena that justify their utility in engineering devices (e.g., band gaps and plasmonic hot spots), they are quite challenging to fabricate [59]. Furthermore, it is now becoming evident that "nearly" periodic devices may have their own compelling properties worthy of consideration in future devices; for instance, the "magic angle" Moiré patterning of multiply layered graphene [60–67]. A simplified model of this phenomenon relevant here is proposed in [66], which studied two mismatched one-dimensional subwavelength photonic crystal slabs that were overlapped (Fig. 1-top). While our model does not permit this sort of patterning, one could imagine approximating this by a triply layered structure with interfaces $z = h + \cos(r\xi)$ and $z = -h + \cos((r+1)\xi)$ (Fig. 1-middle). This currently sits outside of our capabilities, as it requires three layers (a current object of research by the author), but a subsequent approximation can be pondered by sending $h \to 0$ and focusing upon twice the average

$$z = \cos(r\xi) + \cos((r+1)\xi) = \cos(x) + \cos\left(\left(\frac{r+1}{r}\right)x\right)$$

$$= \cos(x) + \cos((1 + 1/r)x),$$

upon setting $x = r\xi$ (Fig. 1-bottom). We consider this profile in the cases $r = 4, 64$ in Section 5.C, and show how this can be simulated in a rapid and reliable manner with our new algorithm.

Of course, the move away from periodicity raises the difficult question of the nature of this generalization, and in this contribution, we investigate a notion of "quasiperiodicity" due to Moser [68]. Wilkening and Zhao [69–72] have taken this approach in the context of the free-surface fluid mechanical water wave problem to a transformative effect. (See also the recent paper [73].) The purpose of this work is to generalize one particular HOPS algorithm, Bruno and Reitich's FE recursions, to the setting of doubly layered media with interfaces shaped by functions which are *quasiperiodic* in this sense. In this initial contribution, we will show how quite complicated configurations with widely disparate or even incommensurate periodicities can be simulated with relative ease using a simple, accurate, and robust reformulation of the governing equations involving dependent variables simply "lifted" to a higher-dimensional torus. We note that our approach is related to the recent contribution of Lou and Fan [67], who proposed a generalization of the RCWA very much in the spirit of this method. While we only address two-layer configurations in two dimensions (TE/TM polarization), we fully intend to generalize our algorithm to multiple layers, the fully vectorial Maxwell equations in three dimensions, and two-dimensional periodic materials such as graphene to simulate the Moiré patterning of current interest.

The paper is organized as follows: in Section 2, we state the equations governing the linear scattering of electromagnetic radiation by a doubly layered structure with a sharp interface. In Section 3, we recall Moser's definition of quasiperiodic functions used in this paper, and in Section 3.A, we specify the generalized Rayleigh expansions for linear waves satisfying these quasiperiodic boundary conditions. In Section 4, we outline the generalizations required for the FE recursions in light of the quasiperiodicity requirements we now demand, while in Section 5, we detail our numerical results. This includes a discussion of algorithmic details for the FE approach in Section 5.A and validation experiments in Section 5.B. In Section 5.C, we discuss a sequence of numerical simulations where we computed the absorbance of radiation incident upon a small, but non-trivial, quasiperiodic interface as a function of interface wavenumber and radiation frequency, thereby constituting a "nonlinear dispersion relation" of SPRs [3–5,74,75]. We provide concluding remarks and discuss future directions in Section 6.

2. GOVERNING EQUATIONS

We consider in this paper structures with the geometry displayed in Fig. 2: a y-invariant, doubly layered structure with an interface, specified by the graph of the function $z = g(x)$, separating two materials. An insulator (with permittivity ϵ^u) fills the region above $z = g(x)$:

$$S^u := \{z > g(x)\},$$

and a second material (with permittivity ϵ^w) occupies

$$S^w := \{z < g(x)\}.$$

(The superscripts are chosen to conform to the notation of the author in previous work [76].) The structure is illuminated from above by monochromatic plane-wave incident radiation of frequency ω and wavenumber $k^u = \sqrt{\epsilon^u}\omega/c_0$ (c_0 is the speed of light) aligned with the grooves:

$$\underline{\mathbf{E}}^i(x, z, t) = \mathbf{A}e^{-i\omega t + i\alpha x - i\gamma^u z}, \quad \underline{\mathbf{H}}^i(x, z, t) = \mathbf{B}e^{-i\omega t + i\alpha x - i\gamma^u z},$$

$$\alpha := k^u \sin(\theta), \quad \gamma^u := k^u \cos(\theta).$$

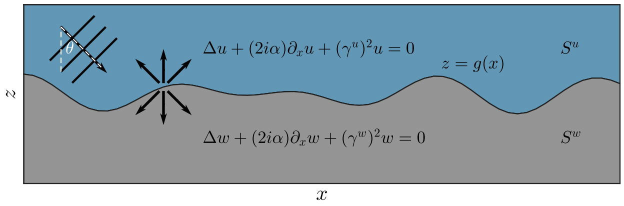

Fig. 2. Two-layer structure with an interface, $z = g(x)$, separating two material layers, S^u and S^w, illuminated by plane–wave incidence.

We consider reduced fields where the time dependence $\exp(-i\omega t)$ and lateral spatial phase $\exp(i\alpha x)$ have been factored out, e.g.,

$$\mathbf{E}(x,z) = e^{i\omega t}e^{-i\alpha x}\underline{\mathbf{E}}(x,z,t), \quad \mathbf{H}(x,z) = e^{i\omega t}e^{-i\alpha x}\underline{\mathbf{H}}(x,z,t),$$

which measure the scattered electric and magnetic fields, respectively. It is well known [77,78] that in this two-dimensional setting, the time-harmonic Maxwell equations decouple into two scalar Helmholtz problems, which govern the transverse electric (TE) and transverse magnetic (TM) polarizations. Denoting the invariant (y) direction of the scattered (electric or magnetic) field in S^u by $u(x,z)$ and S^w by $w(x,z)$, we have

$$\Delta u + 2i\alpha\partial_x u + (\gamma^u)^2 u = 0, \qquad z > g(x), \tag{1a}$$

$$\Delta w + 2i\alpha\partial_x w + (\gamma^w)^2 w = 0, \qquad z < g(x), \tag{1b}$$

where

$$(\gamma^q)^2 = \epsilon^q k_0^2 - \alpha^2, \quad q \in \{u, w\}.$$

While one might expect the classical Helmholtz equation, e.g., $\Delta\tilde{u} + \epsilon^u k_0^2 \tilde{u} = 0$, the phase extraction $u(x,z) = e^{-i\alpha x}\tilde{u}(x,z)$ demands that ∂_x be modified to $\partial_x + i\alpha$, resulting in the "phase extracted" Helmholtz equation (1a). If the invariant direction of the incident radiation is represented by $u^i(x,z)$, then continuity of the fields at the interface demands

$$u - w = \xi, \quad z = g(x), \tag{1c}$$

$$\tau^u\left[\partial_z u - (\partial_x g)\partial_x u - i\alpha(\partial_x g)u\right] - \tau^w\left[\partial_z w - (\partial_x g)\partial_x w - i\alpha(\partial_x g)w\right] = \tau^u \nu, \quad z = g(x), \tag{1d}$$

where the Dirichlet and Neumann data are

$$\xi(x) = -e^{-i\gamma^u g(x)}, \quad \nu(x) = (i\gamma^u + i\alpha(\partial_x g))e^{-i\gamma^u g(x)},$$

and

$$\tau^q = \begin{cases} 1, & \text{TE}, \\ 1/\epsilon^q, & \text{TM}. \end{cases}$$

To close the problem, we specify that the scattered radiation is outgoing: Upward propagating in S^u and downward propagating in S^w.

3. QUASIPERIODIC FUNCTIONS

To investigate the possibility of novel phenomena when plane waves are scattered by grating structures with more general periodicity properties than have been assumed in previous investigations, we entertain the notion of quasiperiodicity. Among many definitions which have been proposed over the years, we select that of Moser [68] and define a function $f(x)$ to be quasiperiodic if

$$f(x) = \tilde{f}(X), \quad X = Kx, \quad x \in \mathbf{R}^d, \quad X \in \mathbf{R}^m, \quad K \in \mathbf{R}^{m\times d},$$

and the envelope function $\tilde{f}(X)$ is *periodic* with respect to the lattice

$$\Gamma = (2\pi\mathbf{Z})^m.$$

In this case, we have the Fourier series representation as

$$\tilde{f}(X) = \sum_{p\in\Gamma'} \hat{f}_p e^{ip\cdot X}, \quad \hat{f}_p = \frac{1}{(2\pi)^m}\int_{P(\Gamma)} \tilde{f}(X)e^{-ip\cdot X}\,\mathrm{d}X,$$

where

$$\Gamma' = \mathbf{Z}^m, \quad P(\Gamma) = [0, 2\pi)^m.$$

We note that if $d = m$ and K is invertible, then the function $f(x)$ is periodic with respect to the lattice induced by K. For later use, we observe that

$$\nabla_x f = K^T \nabla_X \tilde{f}, \quad \Delta_x f = \mathrm{div}_X\left[KK^T\nabla_X\tilde{f}\right].$$

To prescribe a truly non-periodic function, one must specify $m > d$ and that the rows of K be linearly independent over the integers. To investigate this latter point, we consider the case $d = 1$ and $m = 2$, which will be our focus in this work, and select

$$K = (1, q/r)^T, \quad q, r \in \mathbf{Z},$$

featuring rational entries. It is a simple matter to demonstrate that $f(x)$ is $(2\pi r)$-periodic:

$$\begin{aligned} f(x + 2\pi r) &= \tilde{f}(x + 2\pi r, (q/r)(x + 2\pi r)) \\ &= \tilde{f}(x + 2\pi r, (q/r)x + 2\pi q) = \tilde{f}(x, (q/r)x) = f(x). \end{aligned}$$

A simple example of a non-periodic quasiperiodic function (when $d = 1$ and $m = 2$) can be specified by

$$K = (1, \kappa)^T, \quad \kappa \notin \mathbf{Q}.$$

We note that the interface $z = g(x)$ depicted in Fig. 2 is quasiperiodic with $\kappa = \sqrt{2}$; the generating envelope function $\tilde{g}(X) = \tilde{g}(X_1, X_2) = \cos(X_1) + \cos(X_2)$ is shown in Fig. 3 together with the line $X_2 = \kappa X_1 = \sqrt{2}X_1$ along which $\tilde{g}(X)$ is sampled to give $g(x)$.

This notion can be extended to functions that are both laterally quasiperiodic and vertically varying, e.g., $v = v(x, z)$. More specifically, we define such a function to be laterally quasiperiodic if

$$v(x,z) = \tilde{v}(X,z), \quad X = Kx, \quad x \in \mathbf{R}^d, \quad X \in \mathbf{R}^m, \quad K \in \mathbf{R}^{m\times d},$$

and the envelope function $\tilde{v}(X,z)$ is laterally *periodic* with respect to the lattice Γ above. Once again, we have a Fourier series representation

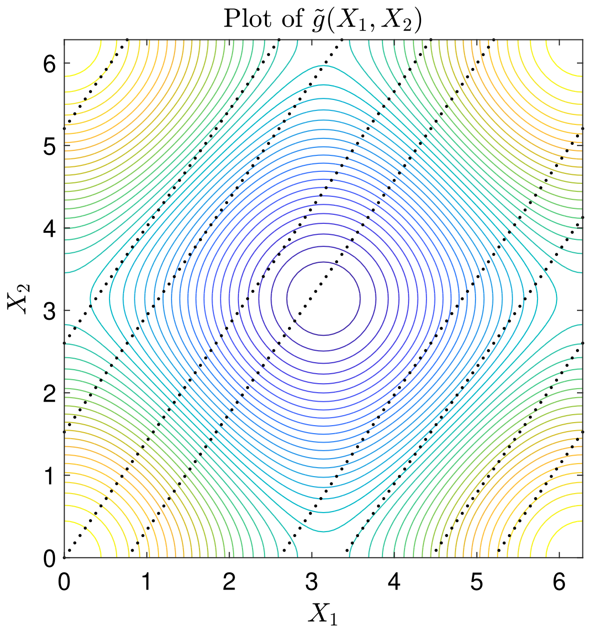

Fig. 3. Contour plot of the envelope function $\tilde{g}(X) = \tilde{g}(X_1, X_2) = \cos(X_1) + \cos(X_2)$ overlaid with the line $X_2 = \kappa X_1 = \sqrt{2} X_1$ along which $z = \tilde{g}(X)$ is sampled to give the interface in Fig. 2.

$$\tilde{v}(X, z) = \sum_{p \in \Gamma'} \hat{v}_p(z) e^{ip\cdot X},$$

$$\hat{v}_p(z) = \frac{1}{(2\pi)^m} \int_{P(\Gamma)} \tilde{v}(X, z) e^{-ip\cdot X} \, \mathrm{d}X.$$

We now assume that the interface $z = g(x) = \tilde{g}(X)$ is quasiperiodic and seek laterally quasiperiodic scattered fields

$$u(x, z) = \tilde{u}(X, z), \quad w(x, z) = \tilde{w}(X, z),$$

satisfying (1). Thus, we require Γ-periodic, upward/downward propagating solutions of

$$\mathrm{div}_X \left[K K^T \nabla_X \tilde{u} \right] + \partial_z^2 \tilde{u} + 2i\alpha K^T \nabla_X \tilde{u} + (\gamma^u)^2 \tilde{u} = 0, \quad z > \tilde{g}(X), \tag{2a}$$

$$\mathrm{div}_X \left[K K^T \nabla_X \tilde{w} \right] + \partial_z^2 \tilde{w} + 2i\alpha K^T \nabla_X \tilde{w} + (\gamma^w)^2 \tilde{w} = 0, \quad z < \tilde{g}(X), \tag{2b}$$

$$\tilde{u} - \tilde{w} = \tilde{\xi}, \quad z = \tilde{g}(X), \tag{2c}$$

$$\tau^u \left[\partial_z \tilde{u} - (K^T \nabla_X \tilde{g}) \cdot (K^T \nabla_X \tilde{u}) - i\alpha (K^T \nabla_X \tilde{g}) \tilde{u} \right] - \tau^w \left[\partial_z \tilde{w} - (K^T \nabla_X \tilde{g}) \cdot (K^T \nabla_X \tilde{w}) - i\alpha (K^T \nabla_X \tilde{g}) \tilde{w} \right] = \tau^u \tilde{v}, \quad z = \tilde{g}(X), \tag{2d}$$

where

$$\tilde{\xi}(X) = -e^{-i\gamma^u \tilde{g}(X)}, \quad \tilde{v}(X) = \left\{ (i\gamma^u) + i\alpha (K^T \nabla_X \tilde{g}) \right\} e^{-i\gamma^u \tilde{g}(X)}.$$

A. Rayleigh Expansions

For our immediate use, we recall the Rayleigh expansions, derived from separation of variables [77,78], which specify the Γ-periodic, upward/downward propagating solutions of (2a) and (2b). More specifically, the Γ-periodic upward propagating solutions of (2a) are

$$\tilde{u}(X, z) = \sum_{p \in \Gamma'} \hat{a}_p e^{ip\cdot X + i\gamma_p^u z}, \quad (X, z) \in P(\Gamma) \times (0, \infty),$$

while the Γ-periodic downward propagating solutions of (2b) can be expressed as

$$\tilde{w}(X, z) = \sum_{p \in \Gamma'} \hat{d}_p e^{ip\cdot X - i\gamma_p^w z}, \quad (X, z) \in P(\Gamma) \times (-\infty, 0),$$

where, for $\alpha \in \mathbf{R}^d$, $p \in \mathbf{Z}^m$, and $q \in \{u, w\}$,

$$\alpha_p := \alpha + K^T p, \quad \gamma_p^q := \sqrt{\epsilon^q k_0^2 - |\alpha_p|^2}, \quad \mathrm{Im}\{\gamma_p^q\} \geq 0.$$

In the case $\epsilon^q \in \mathbf{R}$, we have

$$\gamma_p^q = \begin{cases} \sqrt{\epsilon^q k_0^2 - |\alpha_p|^2}, & p \in \mathcal{U}^q, \\ i\sqrt{|\alpha_p|^2 - \epsilon^q k_0^2}, & p \notin \mathcal{U}^q, \end{cases}$$

and

$$\mathcal{U}^q := \{ p \in \mathbf{Z}^m \mid |\alpha_p|^2 < \epsilon^q k_0^2 \},$$

which are the propagating modes.

In the case of a flat interface, $\tilde{g} \equiv 0$, these Rayleigh expansions can be used to recover the exact solution of (2). The boundary conditions reduce, at each wavenumber $p \in \mathbf{Z}^m$, to

$$\begin{pmatrix} 1 & -1 \\ \tau^u (i\gamma_p^u) & -\tau^w (-i\gamma_p^w) \end{pmatrix} \begin{pmatrix} \hat{a}_p \\ \hat{d}_p \end{pmatrix} = \begin{pmatrix} \hat{\xi}_p \\ \tau^u \hat{v}_p \end{pmatrix}, \tag{3}$$

which can be readily solved to yield

$$\begin{pmatrix} \hat{a}_p \\ \hat{d}_p \end{pmatrix} = \frac{1}{\tau^u (i\gamma_p^u) + \tau^w (i\gamma_p^w)} \begin{pmatrix} \tau^w (i\gamma_p^w) \hat{\xi}_p + \tau^u \hat{v}_p \\ -\tau^u (i\gamma_p^u) \hat{\xi}_p + \tau^u \hat{v}_p \end{pmatrix}. \tag{4}$$

In fact, in this case of planewave incidence

$$\hat{\xi}_0 = -1; \quad \hat{v}_0 = i\gamma^u; \quad \hat{\xi}_p = \hat{v}_p = 0, \quad p \neq 0,$$

we recover

$$\hat{a}_0 = \frac{\tau^u \gamma^u - \tau^w \gamma^w}{\tau^u \gamma^u + \tau^w \gamma^w}; \quad \hat{d}_0 = \frac{2\tau^u \gamma^u}{\tau^u \gamma^u + \tau^w \gamma^w};$$

$$\hat{a}_p = \hat{d}_p = 0, \quad p \neq 0,$$

which are the Fresnel coefficients [77]. As we shall see, this straightforward solution procedure will be repeatedly used as the core of the FE algorithm.

4. METHOD OF FIELD EXPANSIONS

The method of field expansions (FEs) is a perturbative algorithm based upon interfacial deformations of the form $z = \tilde{g}(X) = \varepsilon \tilde{f}(X)$, where, initially, we assume that $\varepsilon \ll 1$.

However, it is important to note that the domain of analyticity of the relevant expansions typically includes a neighborhood of the *entire* real axis (see, e.g., [46,48]), which can be accessed using suitable analytic continuation methods. As we shall see later, the method of Padé approximation [58] is a particularly compelling choice for this task.

In the present context, the FE method begins with the expansions

$$\tilde{u} = \tilde{u}(X, z; \varepsilon) = \sum_{n=0}^{\infty} \tilde{u}_n(X, z)\varepsilon^n,$$

$$\tilde{w} = \tilde{w}(X, z; \varepsilon) = \sum_{n=0}^{\infty} \tilde{w}_n(X, z)\varepsilon^n,$$

and inserts these into (2) and, equating at like orders of ε, results in

$$\operatorname{div}_X\left[KK^T\nabla_X\tilde{u}_n\right] + \partial_z^2\tilde{u}_n + 2i\alpha K^T\nabla_X\tilde{u}_n + (\gamma^u)^2\tilde{u}_n = 0, \quad z > 0, \tag{5a}$$

$$\operatorname{div}_X\left[KK^T\nabla_X\tilde{w}_n\right] + \partial_z^2\tilde{w}_n + 2i\alpha K^T\nabla_X\tilde{w}_n + (\gamma^w)^2\tilde{w}_n = 0, \quad z < 0, \tag{5b}$$

$$\tilde{u}_n - \tilde{w}_n = \tilde{\xi}_n + \tilde{Q}_n, \quad z = 0, \tag{5c}$$

$$\tau^u\partial_z\tilde{u}_n - \tau^w\partial_z\tilde{w}_n = \tau^u\tilde{\nu}_n + \tilde{R}_n, \quad z = 0, \tag{5d}$$

where

$$\tilde{\xi}_n = -(-i\gamma^u)^n\tilde{F}_n,$$

$$\tilde{\nu}_n = (i\gamma^u)\left\{(-i\gamma^u)^n\tilde{F}_n + i\alpha(-i\gamma^u)^{n-1}(K^T\nabla_X\tilde{f})\tilde{F}_{n-1}\right\},$$

and

$$\tilde{Q}_n = -\sum_{\ell=0}^{n}\tilde{F}_{n-\ell}\partial_z^{n-\ell}\tilde{u}_\ell(X, 0) + \sum_{\ell=0}^{n}\tilde{F}_{n-\ell}\partial_z^{n-\ell}\tilde{w}_\ell(X, 0), \tag{6}$$

and

$$\begin{aligned}\tilde{R}_n = &-\tau^u\sum_{\ell=0}^{n}\tilde{F}_{n-\ell}\partial_z^{n-\ell+1}\tilde{u}_\ell(X, 0)\\ &+\tau^u\sum_{\ell=0}^{n-1}\tilde{F}_{n-1-\ell}(K^T\nabla_X\tilde{f})\cdot K^T\nabla_X\partial_z^{n-1-\ell}\tilde{u}_\ell(X, 0)\\ &+\tau^u\sum_{\ell=0}^{n-1}\tilde{F}_{n-1-\ell}(i\alpha)(K^T\nabla_X\tilde{f})\partial_z^{n-1-\ell}\tilde{u}_\ell(X, 0)\\ &+\tau^w\sum_{\ell=0}^{n}\tilde{F}_{n-\ell}\partial_z^{n-\ell+1}\tilde{w}_\ell(X, 0)\\ &-\tau^w\sum_{\ell=0}^{n-1}\tilde{F}_{n-1-\ell}(K^T\nabla_X\tilde{f})\cdot K^T\nabla_X\partial_z^{n-1-\ell}\tilde{w}_\ell(X, 0)\\ &-\tau^w\sum_{\ell=0}^{n-1}\tilde{F}_{n-1-\ell}(i\alpha)(K^T\nabla_X\tilde{f})\partial_z^{n-1-\ell}\tilde{w}_\ell(X, 0),\end{aligned}$$

and

$$\tilde{F}_n(X) = \frac{\tilde{f}(X)^n}{n!}.$$

As we mentioned above, the periodic outgoing solutions of (5a) and (5b) are given by the Rayleigh expansions:

$$\tilde{u}_n(X, z) = \sum_{p\in\Gamma'}\hat{a}_{n,p}e^{ip\cdot X + i\gamma_p^u z},$$

$$\tilde{w}_n(X, z) = \sum_{p\in\Gamma'}\hat{d}_{n,p}e^{ip\cdot X - i\gamma_p^w z}. \tag{7}$$

The boundary conditions (5c) and (5d) allow us to recover the $\{\hat{a}_{n,p}, \hat{d}_{n,p}\}$. It is not difficult to see that, at each perturbation order ε^n and every wavenumber $p \in \mathbf{Z}^m$, we must solve

$$\begin{pmatrix} 1 & -1 \\ \tau^u(i\gamma_p^u) & -\tau^w(-i\gamma_p^w)\end{pmatrix}\begin{pmatrix}\hat{a}_{n,p}\\ \hat{d}_{n,p}\end{pmatrix} = \begin{pmatrix}\hat{\xi}_{n,p} + \hat{Q}_{n,p}\\ \tau^u\hat{\nu}_{n,p} + \hat{R}_{n,p}\end{pmatrix},$$

c.f. (3), which can be readily accomplished via

$$\begin{pmatrix}\hat{a}_{n,p}\\ \hat{d}_{n,p}\end{pmatrix} = \frac{1}{\tau^u(i\gamma_p^u) + \tau^w(i\gamma_p^w)} \times \begin{pmatrix}\tau^w(i\gamma_p^w)(\hat{\xi}_{n,p} + \hat{Q}_{n,p}) + (\tau^u\hat{\nu}_p + \hat{R}_{n,p})\\ -\tau^u(i\gamma_p^u)(\hat{\xi}_{n,p} + \hat{Q}_{n,p}) + (\tau^u\hat{\nu}_p + \hat{R}_{n,p})\end{pmatrix}, \tag{8}$$

c.f. (4).

These formulas, (8), completely specify the FE recursions, though we should comment on the one difficulty, namely the *formation* of the right-hand sides, $\{\hat{Q}_{n,p}, \hat{R}_{n,p}\}$. This can be effectively specified by examining the first term in $\tilde{Q}_n$, (6):

$$\begin{aligned}\tilde{Q}_n^1(X) &= -\sum_{\ell=0}^{n}\tilde{F}_{n-\ell}(X)\partial_z^{n-\ell}\tilde{u}_\ell(X, 0)\\ &= -\sum_{\ell=0}^{n}\left(\sum_{p\in\Gamma'}\hat{F}_{n-\ell,p}e^{ip\cdot X}\right)\left(\sum_{q\in\Gamma'}(i\gamma_q^u)^{n-\ell}\hat{a}_{\ell,q}e^{iq\cdot X}\right)\\ &= -\sum_{\ell=0}^{n}\sum_{p\in\Gamma'}\left(\sum_{q\in\Gamma'}\hat{F}_{n-\ell,p-q}(i\gamma_q^u)^{n-\ell}\hat{a}_{\ell,q}\right)e^{ip\cdot X},\end{aligned}$$

so the Fourier transform of $\tilde{Q}_n^1$ can be expressed in terms of the convolution

$$\hat{Q}_{n,p}^1 = -\sum_{\ell=0}^{n}\sum_{q\in\Gamma'}\hat{F}_{n-\ell,p-q}(i\gamma_q^u)^{n-\ell}\hat{a}_{\ell,q}. \tag{9}$$

5. NUMERICAL RESULTS

At this point, we are in a position to implement, validate, and explore the capabilities of this novel FE method for interfacial shapes that are quasiperiodic. As we shall see, the spectral character of the Rayleigh expansions and the exponential nature of the Taylor series that this algorithm uses will deliver stunning rates of convergence, which make it extremely compelling for many configurations of applied interest. In order to focus the discussion, we restrict to the case of one lateral dimensional, $d = 1$, which is lifted to a two-dimensional torus, $m = 2$, implying that $K \in \mathbf{R}^{2\times 1}$. However, the extension to $d = 2$ and larger m is rather immediate, though the former would require a consideration of the full Maxwell equations.

A. FE Algorithm

The FE algorithm recovers estimates of the Rayleigh–Taylor coefficients $\{\hat{a}_{n,p}, \hat{d}_{n,p}\}$ in the expansions (7) for a finite number of perturbation orders, $0 \le n \le N$, and a finite subset of wavenumbers:

$$\mathbf{P}(N_X) = \{p \in \Gamma' \mid -N_X^j/2 \le p_j \le N_x^j/2 - 1,\ 1 \le j \le 2\}.$$

With these coefficients, the Rayleigh expansions, (7), can be used to recover any quantity of interest, in particular the reflectance and transmittance, which we study presently.

To find these approximations, we resort to techniques borrowed from the family of spectral method algorithms [79–82]. More specifically, we approximate functions

$$\tilde{f}(X) \approx \tilde{f}^{N_X}(X) = \sum_{p \in \mathbf{P}(N_X)} \hat{f}_p e^{ip\cdot X},$$

where

$$p = \begin{pmatrix} p_1 \\ p_2 \end{pmatrix}, \quad X = \begin{pmatrix} X_1 \\ X_2 \end{pmatrix}, \quad N_X = \begin{pmatrix} N_X^1 \\ N_X^2 \end{pmatrix}.$$

It is well-known that, for smooth functions with periodic derivatives, the $\hat{f}_p$ can be computed with great accuracy via the trapezoidal rule. When coupled to established results on the rapid decay of the Fourier coefficients of such functions, their derivatives can be approximated with high fidelity via

$$\nabla_X \tilde{f}(X) \approx \nabla_X \tilde{f}^{N_X}(X) = \sum_{p \in \mathbf{P}(N_X)} (ip) \hat{f}_p e^{ip\cdot X},$$

as can Fourier multipliers such as

$$(i\gamma_D^u)^\ell [\tilde{f}(X)] \approx (i\gamma_D^u)^\ell [\tilde{f}^{N_X}(X)] = \sum_{p \in \mathbf{P}(N_X)} (i\gamma_p^u)^\ell \hat{f}_p e^{ip\cdot X}.$$

We can now simulate the $\{\hat{a}_{n,p}, \hat{d}_{n,p}\}$ by solving (8) at each relevant wavenumber $p \in \mathbf{P}(N_X)$ after forming the right-hand-sides with considerations akin to (9). For this, the derivatives and Fourier multipliers are computed in Fourier space while the convolutions are accomplished with the assistance of the multidimensional FFT algorithm [79–82].

With these coefficients, we form approximations to $\tilde{u}$ and $\tilde{w}$, e.g.,

$$\tilde{u}(X, z; \varepsilon) \approx \tilde{u}^{N_X,N}(X, z) := \sum_{p \in \mathbf{P}(N_X)} a_p^N(\varepsilon) e^{ip\cdot X + i\gamma_p^u z},$$

$$a_p^N(\varepsilon) := \sum_{n=0}^{N} \hat{a}_{n,p} \varepsilon^n, \tag{10}$$

and the question arises: how is the truncated Taylor series in (10) to be summed? As we have observed over the past two decades [46,48,83], Padé summation can be coupled to HOPS algorithms with great success, and we utilize it here. Padé approximation estimates the truncated Taylor series in (10) by the rational function:

$$[L/M](\varepsilon) := \frac{A^L(\varepsilon)}{B^M(\varepsilon)} = \frac{\sum_{\ell=0}^{L} A_\ell \varepsilon^\ell}{1 + \sum_{m=1}^{M} B_m \varepsilon^m}, \quad L + M = N,$$

and

$$[L/M](\varepsilon) = a_p^N(\varepsilon) + \mathcal{O}(\varepsilon^{L+M+1}).$$

Classical formulas for the $\{A_\ell, B_m\}$ are described in [58], and these approximants have noteworthy properties of enhanced convergence and analytic continuation. We refer the interested reader to Section 2.2 of Baker and Graves-Morris [58] and the explicit calculations in Section 8.3 of Bender and Orszag [84] for a complete discussion of capabilities and limitations.

B. Validation

To validate our implementation, we utilized the method of manufactured solutions (MMS) [85–87]. This technique begins with the observation that, in devising a solver for a generic system of partial differential equations and boundary conditions

$$\begin{aligned} \mathcal{P}v &= 0, && \text{in } \Omega, \\ \mathcal{B}v &= 0, && \text{at } \partial\Omega, \end{aligned}$$

it is typically just as easy to construct one for the inhomogeneous problem

$$\begin{aligned} \mathcal{P}v &= \mathcal{R}, && \text{in } \Omega, \\ \mathcal{B}v &= \mathcal{J}, && \text{at } \partial\Omega. \end{aligned}$$

In order to validate a code, one can choose a "manufactured solution," v', and select

$$\mathcal{R}' = \mathcal{P}v', \quad \mathcal{J}' = \mathcal{B}v'.$$

Now, associated to the pair $\{\mathcal{R}', \mathcal{J}'\}$, we have the *exact* solution of the latter problem, v', against which to measure errors. While this test is not definitive, if v' is chosen to have behavior suggested by the original model (e.g., exactly satisfying boundary conditions), then this can give us great confidence in our implementation.

In the current context, we considered the functions

$$\tilde{u}^{\text{exact}}(X, z) := A_r e^{ir\cdot X + i\gamma_r^u z},$$

$$\tilde{w}^{\text{exact}}(X, z) := B_r e^{ir\cdot X - i\gamma_r^w z}, \quad r \in \mathbf{Z}^2,$$

which are outgoing, Γ-periodic solutions of the Helmholtz equations (2a) and (2b), and defined the Dirichlet and Neumann interfacial traces:

$$\tilde{U}^{\text{exact}}(X) := \left[\tilde{u}^{\text{exact}}\right]_{z=\tilde{g}(X)},$$

$$\tilde{W}^{\text{exact}}(X) := \left[\tilde{w}^{\text{exact}}\right]_{z=\tilde{g}(X)},$$

$$\tilde{U}'^{,\text{exact}}(X) := \Big[\partial_z \tilde{u}^{\text{exact}} - (K^T \nabla_X \tilde{g}) \cdot (K^T \nabla_X \tilde{u}^{\text{exact}}) - i\alpha (K^T \nabla_X \tilde{g}) \tilde{u}^{\text{exact}}\Big]_{z=\tilde{g}(X)},$$

$$\tilde{W}'^{,\text{exact}}(X) := \Big[\partial_z \tilde{w}^{\text{exact}} - (K^T \nabla_X \tilde{g}) \cdot (K^T \nabla_X \tilde{w}^{\text{exact}}) - i\alpha (K^T \nabla_X \tilde{g}) \tilde{w}^{\text{exact}}\Big]_{z=\tilde{g}(X)}.$$

We selected TM polarization, physical parameters

$$\epsilon^u = 1.1, \quad \epsilon^w = 1.3, \quad \lambda = 2\pi \quad \theta = 30^\circ, \quad K = (1, \kappa)^T, \quad \kappa = \sqrt{2}, \tag{11}$$

and numerical parameters

$$N_X^1 = N_X^2 = 16, \quad N = 16. \tag{12}$$

To investigate the behavior of our implementation we chose the layer interface

$$\tilde{g}(X) = \varepsilon \tilde{f}(X), \quad \tilde{f}(X) = \cos(X_1)\sin(X_2),$$

three values of ε,

$$\varepsilon = 0.02,\ 0.1,\ 0.15,$$

and MMS parameters

$$r = (1, 1)^T, \quad A_r = -3, \quad B_r = \pi. \tag{13}$$

With these choices, we set

$$\tilde{\xi}_r = \tilde{U}^{\text{exact}} - \tilde{W}^{\text{exact}}, \quad \tilde{\nu}_r = \frac{1}{\tau^u}\left\{\tau^u \tilde{U}'^{,\text{exact}} - \tau^w \tilde{W}'^{,\text{exact}}\right\},$$

and sent these to our implementation, which delivered approximations to the $\{\hat{a}_{n,p}, \hat{d}_{n,p}\}$ that we then used to compute the estimates $\tilde{U}^{\text{approx}}$ and $\tilde{U}'^{,\text{approx}}$. (The results were similar for $\tilde{W}^{\text{approx}}$ and $\tilde{W}'^{,\text{approx}}$). With these, we computed the relative errors, e.g.,

$$\text{Error}_{\text{rel}} = \frac{\left|\tilde{U}^{\text{approx}} - \tilde{U}^{\text{exact}}\right|_{L^\infty}}{\left|\tilde{U}^{\text{exact}}\right|_{L^\infty}}. \tag{14}$$

In Fig. 4 we depict the outcomes of this experiment for a small choice of the perturbation parameter, $\varepsilon = 0.02$. These show the extremely rapid and robust convergence of our method using either Taylor or Padé summation for the upper traces $\{\tilde{U}, \tilde{U}'\}$. In fact, as the vertical axis is logarithmic, we deduce that the rate of convergence is spectral and we effectively achieve machine precision after merely $N = 6$ perturbation orders.

Figure 5 shows the results of our experiments for a moderate choice of the perturbation parameter, $\varepsilon = 0.1$. While requiring more perturbation orders, we notice here again the rapid and steady convergence of our method using either Taylor or Padé summation. Again, we notice a spectral rate of convergence down to machine precision, though it now requires 10–12 perturbation orders.

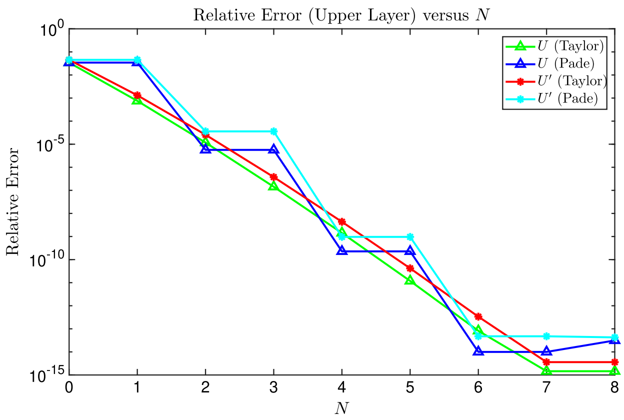

Fig. 4. Plot of the relative error, (14), for a small perturbation ($\varepsilon = 0.02$) in the interfacial data $\{\tilde{U}, \tilde{U}'\}$ using both Taylor and Padé summation. The physical parameters were (11), the numerical discretization was (12), and the MMS values were (13).

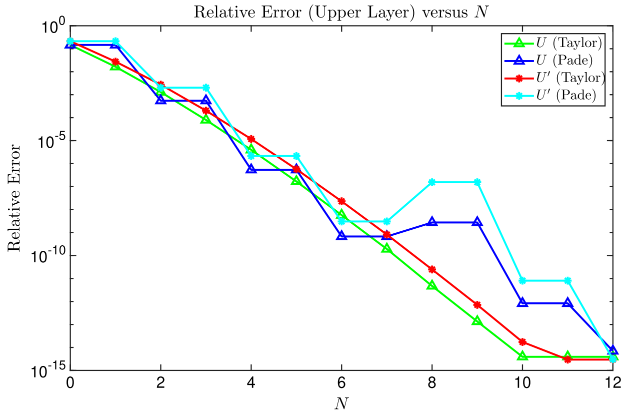

Fig. 5. Plot of the relative error, (14), for a medium perturbation ($\varepsilon = 0.1$) in the interfacial data $\{\tilde{U}, \tilde{U}'\}$ using both Taylor and Padé summation. The physical parameters were (11), the numerical discretization was (12), and the MMS values were (13).

We close with Fig. 6, which summarizes our findings for a quite large choice of the perturbation parameter, $\varepsilon = 0.25$. As above, we see rapid and steady convergence of our method using either Taylor or Padé summation. As with the previous two simulations, we see spectral convergence of our numerical method, though now requiring 12–16 perturbation orders to realize machine precision.

C. Nonlinear Dispersion Relations

With the accuracy and stability of our implementation established, we chose to revisit classical computations from the plasmonics literature [3–5] in light of our new capability of simulating quasiperiodic gratings. In particular, we investigated what we term the "nonlinear dispersion relation" of surface plasmons, which are induced by the weakly nonlinear effect of time-harmonic incident radiation propagating in vacuum, interacting with small interfacial deformations in an infinite layer of silver. (We view the classical linear dispersion relation as

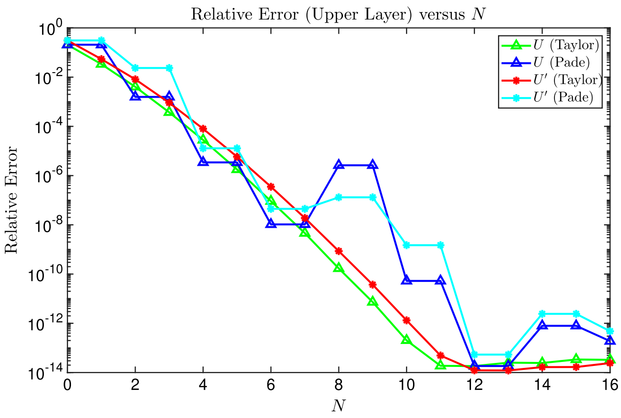

Fig. 6. Plot of the relative error, (14), for a large perturbation ($\varepsilon = 0.25$) in the interfacial data $\{\tilde{U}, \tilde{U}'\}$ using both Taylor and Padé summation. The physical parameters were (11), the numerical discretization was (12), and the MMS values were (13).

involving the propagation of a waveform with a *single* wavenumber [3] in contrast to the configuration we discuss here, where *all* wavenumbers are excited, though the effects of the non-primary wavenumber are vanishingly small [74].)

It is a classical result [88] that time-harmonic (frequency ω), spatially periodic (wavenumber q) electromagnetic plane waves propagating in vacuum must satisfy the linear dispersion relation

$$q = \frac{\omega}{c_0},$$

which we will plot (in solid white) in the forthcoming figures as the "light line." Another well-known relation concerns the propagation of time-harmonic, normally incident ($\theta = 0°$), spatially periodic surface plasmons at a dielectric–metal interface (vacuum–silver in this paper) which must obey [3]

$$q = \frac{\omega}{c_0}\sqrt{\frac{\epsilon^u \epsilon^w}{\epsilon^u + \epsilon^w}}, \qquad \epsilon^w = \epsilon^w(\omega), \tag{15}$$

though, as $\epsilon^w = \epsilon^{\mathrm{Ag}}(\omega) \in \mathbf{C}$ in the classical vacuum–silver configuration we consider, we will plot this relation (in dashed red) with $\mathrm{Re}\{\epsilon^w\}$ replacing ϵ^w. It is this classical result which we attempted to reproduce, and in order to achieve this with our current implementation, we selected a sinusoidal profile:

$$g(x) = \varepsilon f(x), \qquad f(x) = \tilde{f}(Kx), \qquad K = \frac{2\pi}{d}(1, \kappa)^T,$$
$$\tilde{f}(X) = \cos(X_1) + a\cos(X_2), \tag{16}$$

and chose $\varepsilon = 0.01$ in order to excite a surface plasmon; it is well-known that a single *flat* interface cannot generate an SPR [3].

We began with $a = 0$, which corresponds to the classical excitation of an SPR by a single sinusoid [3], focused on TM polarization, chose physical parameters:

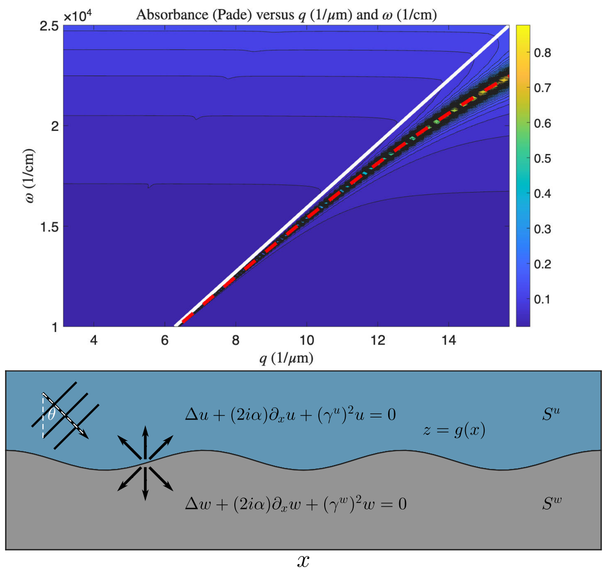

Fig. 7. (Above) Contour plot of absorbance as a function of wavenumber, q (inverse microns), and illumination frequency, ω (inverse centimeters), for a vacuum–silver structure with sinusoidal interface ($a = 0$), (16), of amplitude $\varepsilon = 0.01$ using Padé summation. The solid white line is the light line, and the dashed red line is the dispersion relation for the SPR. The physical parameters were (17) and the numerical discretization was (18). (Below) Plot of the grating structure.

$$\epsilon^u = 1, \quad \epsilon^w = \epsilon^{\mathrm{Ag}}(\omega), \quad 0.400\ \mu\mathrm{m} \le d \le 2.000\ \mu\mathrm{m},$$
$$0.800\ \mu\mathrm{m} \le \lambda \le 2.000\ \mu\mathrm{m}, \tag{17}$$

from which we computed

$$q = 2\pi/d, \qquad \omega = 2\pi c_0/\lambda,$$

and numerical parameters

$$N_X^1 = N_X^2 = 16, \qquad N = 4. \tag{18}$$

In Fig. 7, we show results of our simulations, which displays the absorbance of our structure, $A = 1 - R - T$, where R and T are the reflectance and transmittance [77], respectively, as a function of the wavenumber of the interface and frequency of illumination. We view a spike in absorbance as an indicator of an SPR, as this means that the incident energy is neither reflected nor transmitted, but rather propagating along the insulator–metal interface. Here we see a ridge of values in the range 0.6–0.9 in a sea of quite small (less than 0.1) values, which is exactly overlaid by the dispersion relation for SPRs, (15). This gives us confidence that our code can reproduce this classic result.

We then progressed to a vastly more challenging periodic configuration, which our new formulation can handle with ease. Here the interface features two, widely disparate, periods: d and rd, $r \in \mathbf{Z}$. We made this more precise by choosing the deformation $\tilde{f}$, (16), with $a = 1$ and both $\kappa = 1 + 1/r$, giving

$$f_+(x) = \cos\left(\frac{2\pi x}{d}\right) + \cos\left(\frac{2\pi(r+1)x}{rd}\right),$$

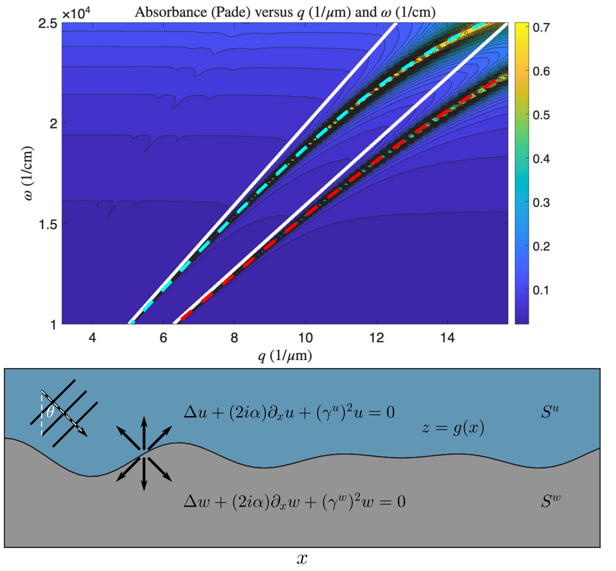

Fig. 8. (Above) Contour plot of absorbance as a function of wavenumber, q (inverse microns), and illumination frequency, ω (inverse centimeters), for a vacuum–silver structure with a sinusoidal interface ($a = 1$, $\kappa = 1 + 1/r$, $r = 4$), (16), of amplitude $\varepsilon = 0.01$ using Padé summation. The solid white line is the light line, and the dashed lines (red and cyan) are the dispersion relations for the SPRs. Physical parameters were (17), and numerical discretization was (18). (Below) Plot of the grating structure.

and $\kappa = 1 - 1/r$, resulting in

$$f_-(x) = \cos\left(\frac{2\pi x}{d}\right) + \cos\left(\frac{2\pi(r-1)x}{rd}\right).$$

The former constitutes a *superharmonic* (period shorter than the base period) perturbation, and the latter a *subharmonic* (period longer than the base) deviation. We found these to be compelling computations as simulations based upon a *periodic* implementation [39] would require $(r N_X^1)$ unknowns for the same spatial accuracy that our code delivers. Clearly, if $r > N_X^1$, our method will enjoy smaller memory requirements and computational complexity, setting aside the issue that numerical methods for PDE typically have deteriorating conditioning properties as the number of spatial discretization points increases [81,89,90].

In Figs. 8 and 9, we depict contour plots of absorbance versus wavenumber and frequency in the case $r = 4$ for superharmonic and subharmonic perturbations, respectively. In contrast to our first results, we now see *two* pronounced ridges of larger absorbance values, each of which can be precisely overlaid with plots of the dispersion relation for SPRs of wavenumber one and either $1 + 1/4$ or $1 - 1/4$. This shows that our implementation can quickly, efficiently, and accurately predict the *two* SPRs which this structure excites.

We revisited these simulations in the more challenging case $r = 64$, which features an interface with periods d and $64d$. In this case, if one is satisfied with, say, 16 gridpoints per period, then a periodic HOPS scheme mandates $N_x = 64 \times 16 = 1024$, while our new scheme only requires $N_X^1 \times N_X^2 = 16 \times 16 = 256$, a factor of four smaller. In Figs. 10 and 11, we display contour plots of absorbance versus wavenumber and frequency in this case $r = 64$ for superharmonic and subharmonic perturbations, respectively. While more difficult

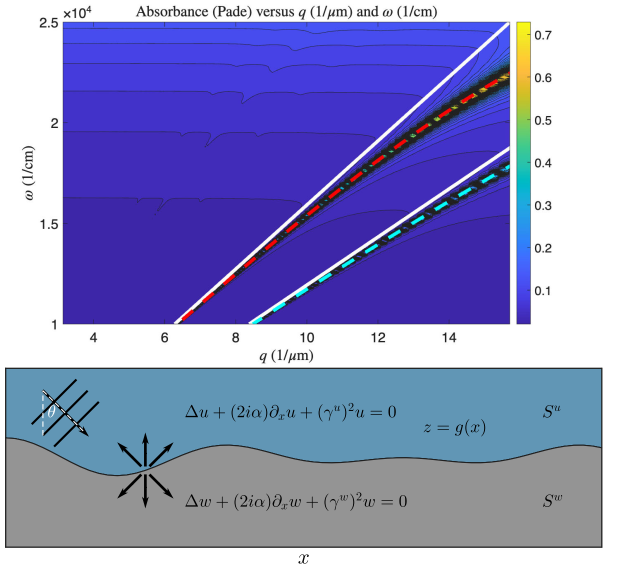

Fig. 9. (Above) Contour plot of the absorbance as a function of wavenumber, q (inverse microns), and illumination frequency, ω (inverse centimeters), for a vacuum–silver structure with sinusoidal interface ($a = 1$, $\kappa = 1 - 1/r$, $r = 4$), (16), of amplitude $\varepsilon = 0.01$ using Padé summation. The solid white line is the light line, and the dashed lines (red and cyan) are the dispersion relations for the SPRs. The physical parameters were (17), and the numerical discretization was (18). (Below) Plot of the grating structure.

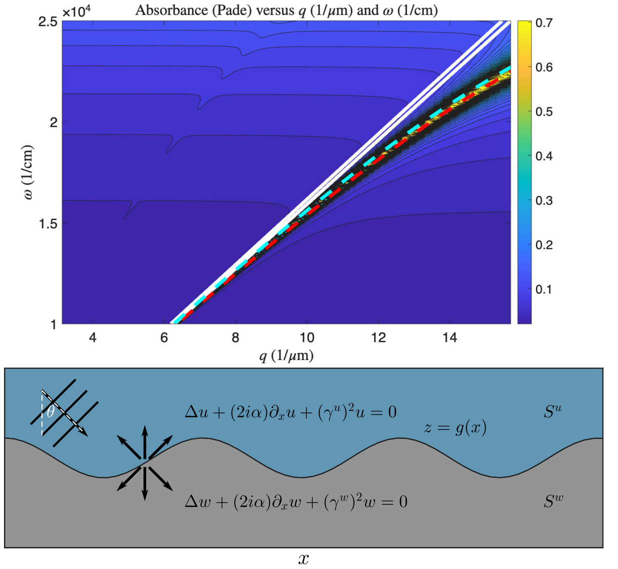

Fig. 10. (Above) Contour plot of absorbance as a function of wavenumber, q (inverse microns), and illumination frequency, ω (inverse centimeters), for a vacuum–silver structure with a sinusoidal interface ($a = 1$, $\kappa = 1 + 1/r$, $r = 64$), (16), of amplitude $\varepsilon = 0.01$ using Padé summation. The solid white line is the light line, and the dashed lines (red and cyan) are the dispersion relations for the SPRs. The physical parameters were (17), and the numerical discretization was (18). (Below) Plot of the grating structure.

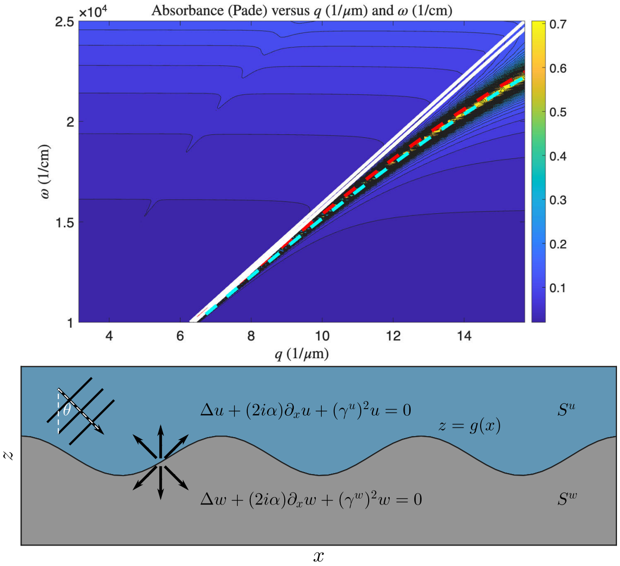

Fig. 11. (Above) Contour plot of the absorbance as a function of wavenumber, q (inverse microns), and illumination frequency, ω (inverse centimeters), for a vacuum–silver structure with a sinusoidal interface ($a = 1$, $\kappa = 1 - 1/r$, $r = 64$), (16), of amplitude $\varepsilon = 0.01$ using Padé summation. The solid white line is the light line, and the dashed lines (red and cyan) are the dispersion relations for the SPRs. The physical parameters were (17), and the numerical discretization was (18). (Below) Plot of the grating structure.

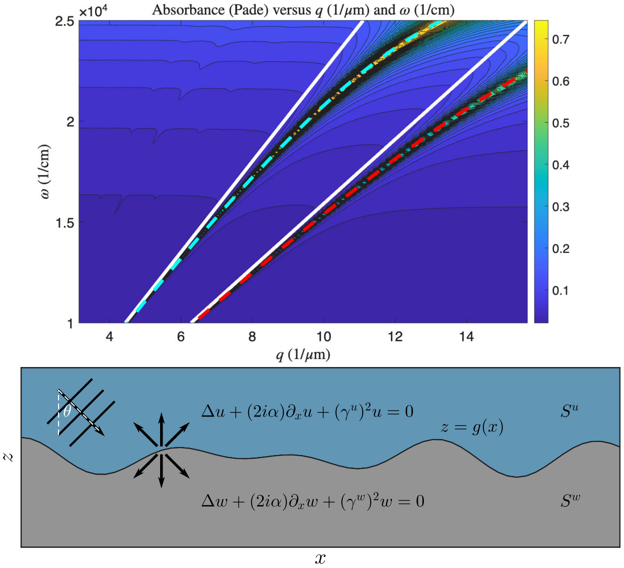

Fig. 12. (Above) Contour plot of the absorbance as a function of wavenumber, q (inverse microns), and illumination frequency, ω (inverse centimeters), for a vacuum–silver structure with a sinusoidal interface ($a = 1$, $\kappa = \sqrt{2}$), (16), of amplitude $\varepsilon = 0.01$ using Padé summation. The solid white line is the light line, and the dashed lines (red and cyan) are the dispersion relations for the SPRs. The physical parameters were (17), and the numerical discretization was (18). (Below) Plot of the grating structure.

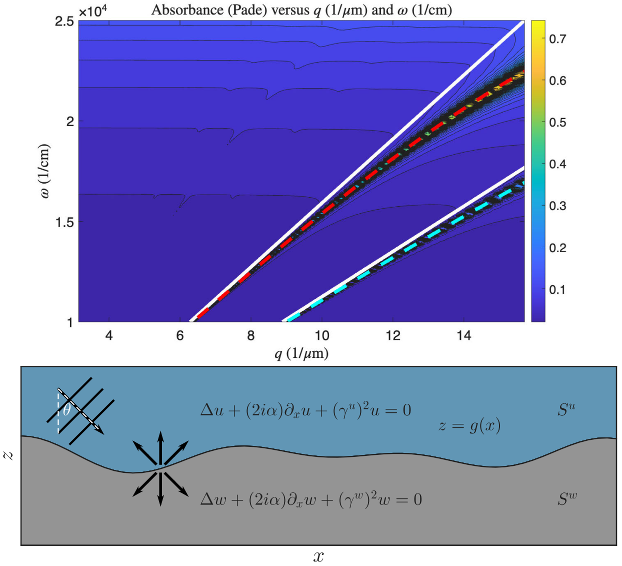

Fig. 13. (Above) Contour plot of the absorbance as a function of wavenumber, q (inverse microns), and illumination frequency, ω (inverse centimeters), for a vacuum–silver structure with a sinusoidal interface ($a = 1$, $\kappa = 1/\sqrt{2}$), (16), of amplitude $\varepsilon = 0.01$ using Padé summation. The solid white line is the light line, and the dashed lines (red and cyan) are the dispersion relations for the SPRs. The physical parameters were (17), and the numerical discretization was (18). (Below) Plot of the grating structure.

to discern due to the closeness of the SPR dispersion relations when the wavenumber changes so slightly. Once again, this shows our implementation to be a rapid and robust method for realizing *both* of these.

To close the discussion of our numerical experiments, we chose a configuration which is *impossible* for a periodic implementation, but which our new algorithm handles seamlessly. To demonstrate this, we chose, in the deformation $\tilde{f}$, (16), with $a = 1$, both $\kappa = \sqrt{2}$ (superharmonic) and $\kappa = 1/\sqrt{2}$ (subharmonic) perturbations. In Figs. 12 and 13, we show absorbance versus wavenumber and frequency, and we notice the two ridges of larger values which can be precisely overlaid with plots of the dispersion relation for SPRs of wavenumbers $\{1, \sqrt{2}\}$ and $\{1, 1/\sqrt{2}\}$, respectively. As we desired, we have an accurate and rapid prediction of SPR dispersion relations for a configuration which is *impossible* for other algorithms to approximate.

6. CONCLUDING REMARKS AND FUTURE DIRECTIONS

In this contribution, the author has derived a novel HOPS scheme for the numerical simulation of scattering returns by doubly layered media with a quasiperiodic interface. The model was implemented and verified, and then used to simulate nonlinear dispersion relations for vacuum–silver structures with quasiperiodic interfaces. The method was shown to be rapid, robust, and reliable and able to address configurations inaccessible to standard algorithms. There are many possible future directions for this work and the author plans to investigate several of these. Paramount is the extension of this algorithm to multiple layers so that the different interfaces can have incommensurate periods, and the generalization of this approach to the fully vectorial three-dimensional Maxwell equations.

Funding. Directorate for Mathematical and Physical Sciences, U.S. National Science Foundation (DMS–2111283).

Acknowledgment. D.P.N. gratefully acknowledges support from the U.S. National Science Foundation.

Disclosures. The author declares no conflicts of interest.

Data availability. Data underlying the results presented in this paper are not publicly available at this time but may be obtained from the author upon reasonable request.

REFERENCES

1. J. D. Joannopoulos, P. R. Villeneuve, and S. Fan, “Photonic crystals: putting a new twist on light,” Nature **386**, 143–149 (1997).
2. J. D. Joannopoulos, S. G. Johnson, J. N. Winn, *et al.*, *Photonic Crystals: Molding the Flow of Light*, 2nd ed. (Princeton University, 2008).
3. H. Raether, *Surface Plasmons on Smooth and Rough Surfaces and on Gratings* (Springer, 1988).
4. S. A. Maier, *Plasmonics: Fundamentals and Applications* (Springer, 2007).
5. S. Enoch and N. Bonod, *Plasmonics: From Basics to Advanced Topics*, Springer Series in Optical Sciences (Springer, 2012).
6. J. Homola, “Surface plasmon resonance sensors for detection of chemical and biological species,” Chem. Rev. **108**, 462–493 (2008).
7. Y. Zhao, X. Hu, G. Chen, *et al.*, “Infrared biosensors based on graphene plasmonics: modeling,” Phys. Chem. Chem. Phys. **15**, 17118 (2013).
8. J.-F. Masson, “Surface plasmon resonance clinical biosensors for medical diagnostics,” ACS Sens. **2**, 16–30 (2017).
9. S.-H. Oh and H. Altug, “Performance metrics and enabling technologies for nanoplasmonic biosensors,” Nat. Commun. **9**, 5263 (2018).
10. A. M. Shrivastav, U. Cvelbar, and I. Abdulhalim, “A comprehensive review on plasmonic-based biosensors used in viral diagnostics,” Commun. Biol. **4**, 70 (2021).
11. J. Wekalao, M. S. Kumaresan, S. Mallan, *et al.*, “Metasurface based surface plasmon resonance (SPR) biosensor for cervical cancer detection with behaviour prediction using machine learning optimization based on support vector regression,” Plasmonics **20**, 4067–4090 (2024).
12. T. Springer, M. Bockova, J. Slaby, *et al.*, “Surface plasmon resonance biosensors and their medical applications,” Biosens. Bioelectron. **278**, 117308 (2025).
13. G. Veronis and S. Fan, “Overview of simulation techniques for plasmonic devices,” in *Surface Plasmon Nanophotonics*, Vol. **131** of Springer Series in Optical Sciences (Springer, 2007), pp. 169–182.
14. B. Gallinet, J. Butet, and O. J. F. Martin, “Numerical methods for nanophotonics: standard problems and future challenges,” Laser Photonics Rev. **9**, 577–603 (2015).
15. A. Taflove and S. C. Hagness, *Computational Electrodynamics: The Finite-Difference Time-Domain Method*, 2nd ed. (Artech House, 2000).
16. R. Rumpf, *Electromagnetic and Photonic Simulation for the Beginner: Finite-Difference Frequency-Domain in MATLAB* (Artech House, 2020).
17. J. Jin, *The Finite Element Method in Electromagnetics*, 2nd ed. (Wiley-Interscience, 2002).
18. K. Busch, M. König, and J. Niegemann, “Discontinuous Galerkin methods in nanophotonics,” Laser Photonics Rev. **5**, 773–809 (2011).
19. R. D. Meade, A. M. Rappe, K. D. Brommer, *et al.*, “Accurate theoretical analysis of photonic band-gap materials,” Phys. Rev. B **48**, 8434–8437 (1993).
20. S. G. Johnson and J. D. Joannopoulos, “Block-iterative frequency-domain methods for Maxwell’s equations in a planewave basis,” Opt. Express **8**, 173–190 (2001).
21. M. G. Moharam and T. K. Gaylord, “Rigorous coupled-wave analysis of planar-grating diffraction,” J. Opt. Soc. Am. **71**, 811–818 (1981).
22. P. Lalanne and G. M. Morris, “Highly improved convergence of the coupled-wave method for TM polarization,” J. Opt. Soc. Am. A **13**, 779–784 (1996).
23. H. Kim, J. Park, and B. Lee, *Fourier Modal Method and its Applications in Computational Nanophotonics* (CRC Press, 2012).
24. B. T. Draine and P. J. Flatau, “Discrete-dipole approximation for scattering calculations,” J. Opt. Soc. Am. A **11**, 1491–1499 (1994).
25. D. Colton and R. Kress, *Inverse Acoustic and Electromagnetic Scattering Theory*, 3rd ed., Vol. **93** of Applied Mathematical Sciences (Springer, 2013).
26. W. Chew, J. Jin, E. Michielssen, *et al.*, *Fast and Efficient Algorithms in Computational Electromagnetics* (Artech House, 2001).
27. Y. Liu, *Fast Multipole Boundary Element Method: Theory and Applications in Engineering* (Cambridge University, 2009).
28. V. Rokhlin, “Rapid solution of integral equations of classical potential theory,” J. Comput. Phys. **60**, 187–207 (1985).
29. L. Greengard and V. Rokhlin, “A fast algorithm for particle simulations,” J. Comput. Phys. **73**, 325–348 (1987).
30. E. Darve and P. Havé, “A fast multipole method for Maxwell equations stable at all frequencies,” Philos. Trans. R. Soc. London A **362**, 603–628 (2004).
31. A. M. Kern and O. J. F. Martin, “Surface integral formulation for 3D simulations of plasmonic and high permittivity nanostructures,” J. Opt. Soc. Am. A **26**, 732–740 (2009).
32. D. M. Milder, “An improved formalism for rough-surface scattering of acoustic and electromagnetic waves,” Proc. SPIE **1558**, 213–221 (1991).
33. D. M. Milder, “An improved formalism for wave scattering from rough surfaces,” J. Acoust. Soc. Am. **89**, 529–541 (1991).
34. D. M. Milder and H. T. Sharp, “Efficient computation of rough surface scattering,” in *Mathematical and Numerical Aspects of Wave Propagation Phenomena (Strasbourg, 1991)* (SIAM, 1991), pp. 314–322.
35. D. M. Milder and H. T. Sharp, “An improved formalism for rough surface scattering. II: numerical trials in three dimensions,” J. Acoust. Soc. Am. **91**, 2620–2626 (1992).
36. D. M. Milder, “Role of the admittance operator in rough-surface scattering,” J. Acoust. Soc. Am. **100**, 759–768 (1996).
37. D. M. Milder, “An improved formalism for electromagnetic scattering from a perfectly conducting rough surface,” Radio Sci. **31**, 1369–1376 (1996).
38. O. Bruno and F. Reitich, “Numerical solution of diffraction problems: a method of variation of boundaries,” J. Opt. Soc. Am. A **10**, 1168–1175 (1993).
39. O. Bruno and F. Reitich, “Numerical solution of diffraction problems: a method of variation of boundaries. II. Finitely conducting gratings, Padé approximants, and singularities,” J. Opt. Soc. Am. A **10**, 2307–2316 (1993).
40. O. Bruno and F. Reitich, “Numerical solution of diffraction problems: a method of variation of boundaries. III. Doubly periodic gratings,” J. Opt. Soc. Am. A **10**, 2551–2562 (1993).
41. O. P. Bruno and F. Reitich, “Calculation of electromagnetic scattering via boundary variations and analytic continuation,” Appl. Comput. Electromagn. Soc. J. **11**, 17–31 (1996).
42. O. P. Bruno and F. Reitich, “Boundary–variation solutions for bounded–obstacle scattering problems in three dimensions,” J. Acoust. Soc. Am. **104**, 2579–2583 (1998).
43. O. P. Bruno and F. Reitich, “High-order boundary perturbation methods,” in *Mathematical Modeling in Optical Science*, Vol. **22** of Frontiers in Applied Mathematics Series (SIAM, 2001), pp. 71–109.
44. D. P. Nicholls and F. Reitich, “A new approach to analyticity of Dirichlet-Neumann operators,” Proc. R. Soc. Edinburgh A **131**, 1411–1433 (2001).
45. D. P. Nicholls and F. Reitich, “Stability of high-order perturbative methods for the computation of Dirichlet-Neumann operators,” J. Comput. Phys. **170**, 276–298 (2001).
46. D. P. Nicholls and F. Reitich, “Analytic continuation of Dirichlet-Neumann operators,” Numer. Math. **94**, 107–146 (2003).
47. D. P. Nicholls and F. Reitich, “Shape deformations in rough surface scattering: cancellations, conditioning, and convergence,” J. Opt. Soc. Am. A **21**, 590–605 (2004).

48. D. P. Nicholls and F. Reitich, "Shape deformations in rough surface scattering: improved algorithms," J. Opt. Soc. Am. A **21**, 606–621 (2004).
49. D. P. Nicholls and F. Reitich, "Boundary perturbation methods for high–frequency acoustic scattering: shallow periodic gratings," J. Acoust. Soc. Am. **123**, 2531–2541 (2008).
50. D. P. Nicholls, "A method of field expansions for vector electromagnetic scattering by layered periodic crossed gratings," J. Opt. Soc. Am. A **32**, 701–709 (2015).
51. Y. He, D. P. Nicholls, and J. Shen, "An efficient and stable spectral method for electromagnetic scattering from a layered periodic structure," J. Comput. Phys. **231**, 3007–3022 (2012).
52. Y. He, M. Min, and D. P. Nicholls, "A spectral element method with transparent boundary condition for periodic layered media scattering," J. Sci. Comput. **68**, 772–802 (2016).
53. Y. Hong and D. P. Nicholls, "A stable high-order perturbation of surfaces method for numerical simulation of diffraction problems in triply layered media," J. Comput. Phys. **330**, 1043–1068 (2017).
54. Y. Hong and D. P. Nicholls, "A high–order perturbation of surfaces method for scattering of linear waves by periodic multiply layered gratings in two and three dimensions," J. Comput. Phys. **345**, 162–188 (2017).
55. Y. Hong and D. P. Nicholls, "A high–order perturbation of surfaces method for vector electromagnetic scattering by doubly layered periodic crossed gratings," J. Comput. Phys. **372**, 748–772 (2018).
56. D. P. Nicholls and J. Shen, "A rigorous numerical analysis of the transformed field expansion method," SIAM J. Numer. Anal. **47**, 2708–2734 (2009).
57. Y. Hong and D. P. Nicholls, "A rigorous numerical analysis of the transformed field expansion method for diffraction by periodic, layered structures," SIAM J. Numer. Anal. **59**, 456–476 (2021).
58. G. A. Baker, Jr. and P. Graves-Morris, *Padé Approximants*, 2nd ed. (Cambridge University, 1996).
59. P. Chengfeng, Z. Shutao, M. Farsari, *et al.*, "Nanofabrication: the unsung hero in enabling advances in nanophotonics," Nanophotonics **12**, 1359–1361 (2023).
60. R. Bistritzer and A. H. MacDonald, "Moiré bands in twisted double-layer graphene," Proc. Natl. Acad. Sci. USA **108**, 12233–12237 (2011).
61. D. Wong, K. P. Nuckolls, M. Oh, *et al.*, "Cascade of electronic transitions in magic-angle twisted bilayer graphene," Nature **582**, 198–202 (2020).
62. E. Andrei, D. Efetov, P. Jarillo-Herrero, *et al.*, "The marvels of Moiré materials," Nat. Rev. Mater. **6**, 201–206 (2021).
63. A. Uri, S. C. de la Barrera, M. T. Randeria, *et al.*, "Superconductivity and strong interactions in a tunable Moiré quasicrystal," Nature **620**, 762–767 (2023).
64. X. Lai, G. Li, A. M. Coe, *et al.*, "Moiré periodic and quasiperiodic crystals in heterostructures of twisted bilayer graphene on hexagonal boron nitride," Nat. Mater. **24**, 1019–1026 (2025).
65. B. Lou, N. Zhao, M. Minkov, *et al.*, "Theory for twisted bilayer photonic crystal slabs," Phys. Rev. Lett. **126**, 136101 (2021).
66. D. X. Nguyen, X. Letartre, E. Drouard, *et al.*, "Magic configurations in moiré superlattice of bilayer photonic crystals: almost-perfect flatbands and unconventional localization," Phys. Rev. Res. **4**, L032031 (2022).
67. B. Lou and S. Fan, "RCWA4D: electromagnetic solver for layered structures with incommensurate periodicities," Comput. Phys. Commun. **306**, 109356 (2025).
68. J. Moser, "On the theory of quasiperiodic motions," SIAM Rev. **8**, 145–172 (1966).
69. J. Wilkening and X. Zhao, "Quasi-periodic travelling gravity–capillary waves," J. Fluid Mech. **915**, A7 (2021).
70. J. Wilkening and X. Zhao, "Spatially quasi-periodic water waves of infinite depth," J. Nonlinear Sci. **31**, 52 (2021).
71. J. Wilkening and X. Zhao, "Spatially quasi-periodic bifurcations from periodic traveling water waves and a method for detecting bifurcations using signed singular values," J. Comput. Phys. **478**, 111954 (2023).
72. J. Wilkening and X. Zhao, "Spatially quasi-periodic water waves of finite depth," Proc. R. Soc. A **479**, 20230019 (2023).
73. D. P. Nicholls, J. Wilkening, and X. Zhao, "Analyticity and stable computation of Dirichlet–Neumann operators for Laplace's equation under quasiperiodic boundary conditions in two and three dimensions," Stud. Appl. Math. **154**, 1–23 (2025).
74. D. P. Nicholls, S.-H. Oh, T. W. Johnson, *et al.*, "Launching surface plasmon waves via vanishingly small periodic gratings," J. Opt. Soc. Am. A **33**, 276–285 (2016).
75. N. Lassaline, R. Brechbühler, S. Vonk, *et al.*, "Optical Fourier surfaces," Nature **582**, 506–510 (2020).
76. D. P. Nicholls, "Three-dimensional acoustic scattering by layered media: a novel surface formulation with operator expansions implementation," Proc. R. Soc. London A **468**, 731–758 (2012).
77. P. Yeh, *Optical Waves in Layered Media* (Wiley-Interscience, 2005), Vol. **61**.
78. G. Bao and P. Li, *Maxwell's Equations in Periodic Structures*, Vol. **208** of Applied Mathematical Sciences (Springer/Science, 2022).
79. D. Gottlieb and S. A. Orszag, *Numerical Analysis of Spectral Methods: Theory and Applications*, Vol. **26** of CBMS-NSF Regional Conference Series in Applied Mathematics (Society for Industrial and Applied Mathematics, 1977).
80. C. Canuto, M. Y. Hussaini, A. Quarteroni, *et al.*, *Spectral Methods in Fluid Dynamics* (Springer-Verlag, 1988).
81. J. P. Boyd, *Chebyshev and Fourier Spectral Methods*, 2nd ed. (Dover, 2001).
82. J. Shen, T. Tang, and L.-L. Wang, *Spectral Methods: Algorithms, Analysis and Applications*, Vol. **41** of Springer Series in Computational Mathematics (Springer, 2011).
83. D. P. Nicholls, "A high–order spectral algorithm for the numerical simulation of layered media with uniaxial hyperbolic materials," J. Comput. Phys. **453**, 110961 (2022).
84. C. M. Bender and S. A. Orszag, *Advanced Mathematical Methods for Scientists and Engineers*, International Series in Pure and Applied Mathematics (McGraw-Hill Book, 1978).
85. O. R. Burggraf, "Analytical and numerical studies of the structure of steady separated flows," J. Fluid Mech. **24**, 113–151 (1966).
86. P. J. Roache, "Code verification by the method of manufactured solutions," J. Fluids Eng. **124**, 4–10 (2002).
87. C. J. Roy, "Review of code and solution verification procedures for computational simulation," J. Comput. Phys. **205**, 131–156 (2005).
88. J. D. Jackson, *Classical Electrodynamics*, 2nd ed. (Wiley, 1975).
89. R. J. LeVeque, *Finite Difference Methods for Ordinary and Partial Differential Equations: Steady-State and Time-Dependent Problems* (Society for Industrial and Applied Mathematics, 2007).
90. M. S. Gockenbach, *Understanding and Implementing the Finite Element Method* (Society for Industrial and Applied Mathematics, 2006).